Attributing Historical and Future Evolution of Radiative Feedbacks to Regional Warming Patterns using a Green's Function Approach: The Preeminence of the Western Pacific

Yue Dong[1], Cristian Proistosescu[2], Kyle C. Armour[1,3], David S. Battisti[1]

[1]*Department of Atmospheric Sciences, University of Washington, Seattle, Washington*
[2]*Joint Institute for the Study of the Atmosphere and the Ocean, University of Washington, Seattle, Washington*
[3]*School of Oceanography, University of Washington, Seattle, Washington*

Corresponding Author: Yue Dong (dongy24@uw.edu)

Abstract

Global radiative feedbacks have been found to vary in global climate model (GCM) simulations. Atmospheric GCMs (AGCMs) driven with historical patterns of sea-surface temperatures (SST) and sea-ice concentrations produce radiative feedbacks that trend toward more negative values, implying low climate sensitivity, over recent decades. Freely-evolving coupled GCMs driven by increasing CO_2 produce radiative feedbacks that trend toward more positive values, implying increasing climate sensitivity, in the future. While this time-variation in feedbacks has been linked to evolving SST patterns, the role of particular regions has not been quantified. Here, a Green's function is derived from a suite of simulations within an AGCM (NCAR's CAM4), allowing an attribution of global feedback changes to surface warming in each region.

The results highlight the radiative response to surface warming in ascent regions of the western tropical Pacific as the dominant control on global radiative feedback changes. Historical warming from the 1950s to 2000s preferentially occurred in the western Pacific, yielding a strong global outgoing radiative response at the TOA and producing a strongly negative global feedback. Long-term warming in coupled GCMs occurs preferentially in tropical descent regions and in high latitudes, where surface warming yields small global TOA radiation changes, and thus a less-negative global feedback. These results illuminate the importance of determining mechanisms of warm pool warming for understanding how feedbacks have varied historically and will evolve in the future.

1. Introduction

In the traditional global energy budget framework (e.g., Gregory et al. 2004; Andrews et al. 2012), the net global top-of-atmosphere (TOA) radiation imbalance, ΔQ, is given by the sum of the radiative forcing, ΔF, and the radiative response to a change in global surface temperature:

$$\Delta Q = \Delta F + \lambda \Delta T, \tag{1}$$

where ΔT is the change in global-mean near-surface air temperature; the radiative feedback parameter λ (units of $\mathrm{Wm^{-2}K^{-1}}$) represents the sum of Planck response and feedbacks associated with changing atmospheric lapse rate, water vapor, clouds and surface albedo. The net global feedback is negative in a stable climate, with a more negative value implying that the Earth needs to warm less to balance an imposed radiative forcing. The net feedback determines the equilibrium climate sensitivity (ECS) – the steady-state ($\Delta Q = 0$) global-mean near-surface air temperature change in response to a doubling of atmospheric CO_2 concentration. That is, $\mathrm{ECS} = -\Delta F_{2x}/\lambda_{eq}$, where ΔF_{2x} is the radiative forcing from CO_2 doubling and λ_{eq} represents the radiative feedback acting in that equilibrium state. Historical energy budget constraints are commonly used to estimate climate sensitivity (e.g., Otto et al. 2013; Knutti et al. 2017), producing an *inferred* climate sensitivity (ICS):

$$\mathrm{ICS} = -\frac{\Delta F_{2x}}{\lambda}, \tag{2}$$

where λ represents the radiative feedbacks associated with transient warming. The use of ICS to estimate ECS depends crucially on the assumption that radiative feedbacks in the distant future will have the same value as those in operation today, i.e., that λ at any given time is equal to λ_{eq} (Armour et al. 2013; Armour 2017; Proistosescu and Huybers. 2017; Marvel et al. 2018; Andrews et al. 2018).

However, this assumption generally does not hold true within simulations using state-of-the-art global climate models (GCMs). Fully-coupled GCMs driven by increased CO_2 forcing tend to show λ evolving toward less negative values, implying a higher value of ICS (Murphy 1995; Senior and Mitchell 2000; Andrews et al. 2012; Williams et al. 2008; Winton et al. 2010; Armour et al. 2013; Andrews et al. 2015; Ceppi and Gregory 2017; Armour 2017; Proistosescu and Huybers 2017; Marvel et al. 2018). On the other hand, atmospheric GCMs (AGCMs) driven with observed historical sea-surface temperature (SST) and sea-ice concentration (SIC) patterns show that λ can vary substantially between decades and that it tends to evolve towards more negative values, corresponding to lower values of ICS, in the latter part of the historical record (Gregory and Andrews 2016; Zhou et al. 2016; Silvers et al. 2018; Andrews et al. 2018; Marvel et al. 2018). Consequentially, extrapolating feedback values from historical energy constraints leads to ICS estimates that are biased low compared to ECS values projected by fully coupled models (Andrews et al. 2018).

We illustrate both historical and future feedback changes here (Fig. 1) within NCAR's Community Atmosphere Model version 4.0 (CAM4; Neale et al. 2010), the atmospheric component of the Community Climate System Model version 4.0 (CCSM4). The historical simulation, hereafter referred to as the *Historical* run, shows the results of CAM4 forced by observed historical SST/SIC patterns (Hurrel et al. 2008, see Table 1). The future simulation, hereafter referred to as the $4\times CO_2$ run, shows the results of CAM4 driven by the evolving SST/SIC anomaly patterns (relative to pre-industrial) produced by the freely-running parent coupled GCM (CCSM4) under abrupt CO_2 quadrupling, performed as part of the Coupled Model Intercomparison Project Phase 5 (CMIP5). In both experiments, all forcing agents (aerosols, greenhouse gases, etc.) are fixed to a present-day (year 2000) level (i.e., $\Delta F = 0$). This allows us to diagnose radiative feedbacks directly from changes in global TOA radiation and near-surface air temperature (TAS), and to attribute any feedback changes to evolving SST/SIC patterns. (See Table 1 for additional details.) In both cases, net TOA radiation becomes increasingly negative with time as increasing TAS drives enhanced outgoing radiative fluxes (Fig. 1 a, b, d, e). However, the global feedback, calculated as annual-global-mean net TOA flux change divided by annual-global-mean TAS change, becomes more negative with time in the *Historical* simulation, relative to mid-century (1950s) values. Meanwhile, radiative feedbacks become less negative with time in the $4\times CO_2$ run (Fig. 1 c, f). From Eq. (2), these feedback values give low ICS in recent decades in the *Historical* run, but higher ICS in the future in the $4\times CO_2$ run, consistent with aforementioned previous studies (e.g., Armour 2017, Proistosescu and Huybers 2017, Andrews et al. 2018, Marvel et al. 2018). Importantly, this different feedback behavior between historical and future warming occurs within the exact same AGCM and thus arises only from the different SST/SIC patterns in the two simulations. A key question is, what about the historical and future warming patterns drives these distinct feedback changes?

Recent studies have argued that feedbacks are sensitive to evolving spatial patterns of surface warming, yet the underlying mechanisms accounting for this so-called *pattern effect* (Stevens et al. 2016) are not clearly established. Armour et al. (2013) proposed a local feedback framework, wherein local TOA radiation change is assumed to be determined by only local surface warming. The net global feedback then varies as the evolving pattern of surface warming modifies the spatial weighting of constant local feedbacks. However, this local feedback framework has been challenged by recent studies pointing to the importance of remote warming on tropospheric stability and low cloud changes, particularly within the tropics (Rose et al. 2014; Rose and Rayborn 2016; Zhou et al. 2016; Mauritsen 2016; Ceppi and Gregory 2017; Andrews et al. 2015; Andrews and Webb 2017; Zhou et al. 2017; Silvers et al. 2018). For example, Zhou et al. (2016) linked the strength of the cloud feedback to the strength of the zonal SST gradient in the tropical Pacific Ocean. In this view, the increasingly negative cloud feedback in recent decades of the historical record can be linked to the cooling in the east Pacific relative to the west Pacific, which gives rise to increased lower tropospheric stability, thereby increasing low cloud amount and reflected shortwave (SW) radiation. The change in this east-west Pacific SST gradient also appears to be important for long-term feedback changes under CO_2 forcing, which favors east Pacific warming that would instead reduce low clouds and drive positive cloud feedback (Andrews et al. 2015; Ceppi and Gregory 2017; Andrews and Webb 2017; Zhou et al. 2017). In addition to the tropical Pacific, Silvers et al. (2018) suggested an important role for trade wind regions as a whole, including the tropical Atlantic. Yet other studies argued that it is the slow emergence of Southern Ocean warming (Armour et al. 2016) that gives rise to more positive feedbacks on centennial timescales (Senior and Mitchell 2000; Armour et al. 2013; Li et al. 2013; Winton et al. 2010; Rose et al. 2014; Rose and Rayborn 2016).

In Fig. 2, we show the changes in SST patterns from the early period to the late period in our AGCM simulations. That is, the SSTs averaged over the 2000s minus that over the 1950s in the *Historical* run, and the SSTs averaged over the last 20 years minus that over the first 20 years in the $4\times CO_2$ run. Both the zonal (east – west) Pacific SST gradient and meridional (extratropics –tropics) SST gradient are decreased in the $4\times CO_2$ run relative to the *Historical* run, with strong east Pacific and high latitude warming at both poles eventually emerging under CO_2 forcing but not yet in the historical record. However, none of the previous approaches have been able to quantify the relative contribution of surface warming in these individual regions to the total change in global feedback, as they only diagnose feedback changes associated with full SST patterns.

The primary goals of this study are to attribute global feedback changes to specific regions of surface warming, and to identify the key mechanisms at work over different periods. To do that, we use a Green's function approach to study the effect of regional SSTs on net TOA radiation, TAS, and feedbacks, respectively. The paper is organized as follows: section 2 proposes a global feedback framework and a Green's function approach. Section 3 illustrate the structure of the Green's function by showing the global response to localized warming. Section 4 validates the Green's function approach within the above AGCM simulations. Section 5 attributes global feedback change to regional warming, for the *Historical* run and the *4×CO₂* run. Section 6 discusses the caveats and broader implications.

2. Formulating feedback dependence on warming patterns

The Green's function approach assumes that the climate response to a prescribed large-scale SST/SIC pattern is a linear combination of the responses to prescribed SST/SIC changes at each location. This enables us to estimate TOA radiation response and TAS response to a full global SST pattern, based on the sensitivity of the responses to regional SST change (section 2a). We derive the Green's function by computing the dependence of TOA radiation and TAS on regional SST/SIC anomalies, from a suite of simulations within CAM4, each with a localized patch of SST and/or SIC anomalies (section 2b).

a. Global feedback framework

By convention, the net global radiative feedback is defined as the change in global-mean net TOA radiative response to warming divided by the change in global-mean TAS:

$$\lambda(t) = \frac{\overline{\mathbf{R}}}{\overline{\mathbf{T}}}, \tag{3}$$

where the overbar denotes the area-weighted global means; **R** represents a vector of changes in local net TOA flux ($\mathbf{R} = [\Delta R_1, \dots, \Delta R_n]$); **T** represents a vector of changes in local TAS ($\mathbf{T} = [\Delta T_1, \dots, \Delta T_n]$); *n* denotes the total number of grid points in the global domain. We define all local responses as a function of time-dependent global SST changes ($\mathbf{T_{SST}}(t) = [\Delta SST_1, \dots, \Delta SST_n]$). That is, for any grid box *i*, the local radiation change (ΔR_i) and the local TAS change (ΔT_i) can be expressed by a first-order Taylor series with respect to SST change at all grid boxes *j* over the ocean domain:

$$\Delta R_i = \sum_j^n \frac{\partial R_i}{\partial SST_j} \Delta SST_j + \varepsilon_R, \ \Delta T_i = \sum_j^n \frac{\partial T_i}{\partial SST_j} \Delta SST_j + \varepsilon_T, \tag{4}$$

where the error term ε_R and ε_T come from potential nonlinearities or residuals that are independent of SSTs. We can then rewrite the vector of TOA radiation change as

$$\mathbf{R} = \boldsymbol{\mathcal{J}}_{\mathbf{R}}\ \mathbf{T}_{\mathbf{SST}}(t), \tag{5}$$

where $\boldsymbol{\mathcal{J}}_{\boldsymbol{R}}$ is a Jacobian matrix, representing the sensitivity of regional ΔR on regional ΔSST:

$$\boldsymbol{\mathcal{J}}_{\boldsymbol{R}} = \begin{pmatrix} \frac{\partial R_1}{\partial SST_1} & \cdots & \frac{\partial R_1}{\partial SST_n} \\ \vdots & \ddots & \vdots \\ \frac{\partial R_n}{\partial SST_1} & \cdots & \frac{\partial R_n}{\partial SST_n} \end{pmatrix}. \tag{6}$$

Likewise, the vector of TAS change can also be reformulated as

$$\mathbf{T} = \boldsymbol{\mathcal{J}}_{\boldsymbol{T}}\ \mathbf{T}_{\mathbf{SST}}(t)\,, \tag{7}$$

where $\boldsymbol{\mathcal{J}}_{\boldsymbol{T}}$ is the Jacobian of regional ΔT with respect to regional ΔSST:

$$\boldsymbol{\mathcal{J}}_{\boldsymbol{T}} = \begin{pmatrix} \frac{\partial T_1}{\partial SST_1} & \cdots & \frac{\partial T_1}{\partial SST_n} \\ \vdots & \ddots & \vdots \\ \frac{\partial T_n}{\partial SST_1} & \cdots & \frac{\partial T_n}{\partial SST_n} \end{pmatrix}. \tag{8}$$

Once we calculated each components of the Jacobians (see next section), substituting Eq. (5) and Eq. (7) into Eq. (3) gives us the final formulation of time-varying global feedback:

$$\lambda(t) = \frac{\overline{\boldsymbol{\mathcal{J}}_{\boldsymbol{R}}\ \mathbf{T}_{\mathbf{SST}}(t)}}{\overline{\boldsymbol{\mathcal{J}}_{\boldsymbol{T}}\ \mathbf{T}_{\mathbf{SST}}(t)}}\,. \tag{9}$$

In this framework, global radiative feedbacks are determined by (i) the sensitivity of local and remote TOA radiation and TAS responses to regional SST changes (i.e., the Jacobians $\boldsymbol{\mathcal{J}}_{\boldsymbol{R}}$ and $\boldsymbol{\mathcal{J}}_{\boldsymbol{T}}$, quantifying the "state dependence"), and (ii) time-varying global SST changes (i.e., $\mathbf{T}_{\mathbf{SST}}(t)$, quantifying the "time dependence"). That is, the apparent time-variation of radiative feedbacks arises from their time-invariant dependence on the SST/SIC state which itself evolves over time (Armour et al. 2013; Stevens et al. 2016; Rose and Rayborn 2016; Proistosescu and Huybers 2017; Goosse et al., 2018). This framework enables us to systematically examine the change in feedback in response to the spatial and temporal evolution of SSTs.

b. The Green's function and experiment design

We derive the sensitivity Jacobians $\boldsymbol{\mathcal{J}_R}$ and $\boldsymbol{\mathcal{J}_T}$ from a suite of AGCM simulations within CAM4, following the set-up in Zhou et al. (2017), who employed a Green's function approach to study the dependence of cloud feedback on SSTs over global ice-free regions using CAM5.3 (Neale at al., 2012). Here, we extend the analysis to include sea-ice covered regions, examine the net feedback, and also decompose total feedback changes into individual components by use of radiative kernels (Shell et al. 2008).

Using CAM4 at 1.9° latitude × 2.5° longitude resolution, we performed 137 fixed-SST simulations, each with a localized patch of anomalous SST and/or SIC (Fig. 3). All simulations are run for 40 years, branched from the 5th year of a control simulation (noted as the *Control* run), which is run for 45 years (Table 1). The *Control* run uses monthly varying observed climatological SST/SIC at present-day level (averaged over years 1982-2001), and all forcing agents are held constant at year 2000 levels. For each experiment, we add a single patch of warm SST anomaly to the monthly climatology, following the form proposed by Barsugli and Sardeshmukh (2002) and Zhou et al. (2017) as:

$$\Delta SST(lat, lon) = Acos^2\left(\frac{\pi}{2}\frac{lat - lat_p}{lat_w}\right)cos^2\left(\frac{\pi}{2}\frac{lon - lon_p}{lon_w}\right), \tag{10}$$

where *A* is the amplitude of the SST anomaly; subscript *p* denotes the center point of the patch and subscript *w* denotes the half-width of the patch. Each SST patch is confined within a rectangular area ($lat_p \pm lon_w, lat_p \pm lon_w$). To cover the global ocean areas efficiently, we set $lon_w = 40°$ for all patches, and set different lat_w as follows: $lat_w = 15°$ in tropical regions ($|lat_p| \leq 30°$) and $lat_w = 25°$ in polar regions ($50° \leq |lat_p| \leq 70°$); patches in mid-latitudes ($30° < |lat_p| < 50°$) are set to have $lat_w = 15°$ on the equatorial side and $lat_w = 25°$ on the polar side of the center point, to be consistent with adjacent patches. All patches are staggered to each other by half-width.

We set the amplitude of SST anomaly *A* to 1.5 K for all patches except for polar patches, where we increase *A* to 3 K, in order to increase the statistical significance of the response to high latitude warming. The amplitudes of our warming patches are smaller than those in Zhou et al. (2017) (where *A* was +4K for warm anomaly and -4K for cold anomaly), but our simulations are carried out with a longer period (40 years each instead of 6 years each). In addition, we perturb SIC along with SSTs within regions covered by sea ice: SIC anomalies within each individual patch follow the same cosine hump as Eq. (10), with the amplitude of SIC anomaly *A* being -20% (SIC is set to be zero wherever the adjusted SIC falls below 0).

By analyzing the response from single-patch experiments, we are able to calculate each component of the sensitivity Jacobians ($\boldsymbol{\mathcal{J}_R}_{ij} = \frac{\partial R_i}{\partial SST_j}$ and $\boldsymbol{\mathcal{J}_T}_{ij} = \frac{\partial T_i}{\partial SST_j}$). The calculation is similar to that of Zhou et al. (2017), but we apply the Jacobian formulation to both net TOA radiation and TAS, while Zhou et al. (2017) only applied the Green's function to TOA radiation from clouds. The net TOA radiation response and TAS response used to calculate the Jacobians are the anomalies relative to the *Control* run averaged over the last 39 years (excluding the first year to allow for atmospheric adjustment). In calculating the Jacobians, grid boxes whose anomalies are not statistically different from zero at 99% confidence level are set to zero. We calculate the sensitivity of local radiative response to SST change within a certain patch *p* as:

$$\left(\frac{\partial R_i}{\partial SST_j}\right)_p = \frac{\Delta R_i}{\Delta SST_p}\frac{a_j}{a_p}, \tag{11}$$

where ΔR_i is net TOA flux anomaly in grid box *i*; ΔSST_p is the area-weighted averaged SST anomaly over the patch *p*; a_j is the surface area of the grid box *j* inside the patch p; and a_p is the total ocean area of the patch *p*. The fact that grid *i* and *j* are two independent points enables this formulation to capture the remote effects of SST change. Given that one grid box is covered by up to 8 patches staggered to each other, weighting all associated patches based on the value of SST anomaly leads to the final form of $\frac{\partial R_i}{\partial SST_j}$:

$$\frac{\partial R_i}{\partial SST_j} = \frac{\sum_p \Delta SST_j \left(\frac{\partial R_i}{\partial SST_j}\right)_p}{\sum_p \Delta SST_j}, \tag{12}$$

where ΔSST_j is the SST anomaly in the grid *j* within the patch *p*, and the summation is over all patches that cover the grid *j*. We can thus derive all components in the sensitivity Jacobians $\boldsymbol{\mathcal{J}_R}$ and $\boldsymbol{\mathcal{J}_T}$ ($\boldsymbol{\mathcal{J}_T}$ follows the same procedures by replacing ΔR with ΔT), and then reconstruct the feedback response to any given SST patterns, assuming that the responses added linearly (we will verify this assumption in the following section).

Although not explicit, this approach includes the effect of sea-ice changes, since SIC anomalies are prescribed at the rate of -20% per +3K within sea-ice covered regions. This parameterized rate, however, may not accurately capture the actual sea-ice changes with warming. Therefore, we add supplementary terms to Eq. (9) to reconstruct the feedback response to a given SST/SIC anomaly pattern, namely, $\mathbf{R}^*$ and $\mathbf{T}^*$, a vector of changes in local net TOA flux and a vector of changes in local TAS that both are associated with sea-ice underestimate. $\mathbf{R}^*$ and $\mathbf{T}^*$ are defined as:

$$\mathbf{R}^* = \boldsymbol{\mathcal{J}_R}^*\mathbf{SIC}^*(t), \mathbf{T}^* = \boldsymbol{\mathcal{J}_T}^*\mathbf{SIC}^*(t), \tag{13}$$

where $\mathbf{SIC}^*(t) = [\Delta SIC_1^*, \dots, \Delta SIC_n^*]$, is a vector representing local sea-ice changes in a particular warming pattern that are not captured by the Green's function at the rate of -20% per +3K; $\boldsymbol{\mathcal{J}_R}^*$ and $\boldsymbol{\mathcal{J}_T}^*$ are the sensitivity Jacobians calculated with respect to SIC change:

$$\boldsymbol{\mathcal{J}_R}^* = \begin{pmatrix} \frac{\partial R_1}{\partial SIC_1} & \cdots & 0 \\ \vdots & \ddots & \vdots \\ 0 & \cdots & \frac{\partial R_n}{\partial SIC_n} \end{pmatrix}, \tag{14}$$

$$\boldsymbol{\mathcal{J}_T}^* = \begin{pmatrix} \frac{\partial T_1}{\partial SIC_1} & \cdots & 0 \\ \vdots & \ddots & \vdots \\ 0 & \cdots & \frac{\partial T_n}{\partial SIC_n} \end{pmatrix}. \tag{15}$$

Unlike the aforementioned full Jacobians, $\boldsymbol{\mathcal{J}_R}^*$ and $\boldsymbol{\mathcal{J}_T}^*$ contains only diagonal terms, i.e., $\frac{\partial R_i}{\partial SIC_j} = 0, \frac{\partial T_i}{\partial SIC_j} = 0\ (if\ i \neq j)$, representing local TOA radiation and local TAS responses to local SIC change. This is motivated by the fact that the response to SIC change is largely localized (see Fig. 4d and Fig. 5e in section 3). This formulation also allows us to keep track of the state dependence of feedback on global SST patterns. Finally, we reconstruct the global radiative feedback as

$$\lambda(t) = \frac{\overline{\boldsymbol{\mathcal{J}_R}\,\mathbf{T_{SST}}(t) + \alpha\boldsymbol{\mathcal{J}_R}^*\mathbf{SIC}^*(t)}}{\overline{\boldsymbol{\mathcal{J}_T}\,\mathbf{T_{SST}}(t) + \alpha\boldsymbol{\mathcal{J}_T}^*\mathbf{SIC}^*(t)}}, \tag{16}$$

where α is a coefficient scaling up SIC changes relative to SST changes in order to compensate the underestimate of SIC in the Green's function, and its value is empirically chosen to be 0.1.

To estimate the annual mean response using Eq. (16), we first calculate 3-month seasonal means and then average across the year. This is necessary because, although the SST/SIC anomalies imposed are constant over a year, the response to the SST/SIC forcing varies as the mean state changes over the seasonal cycle. For example, shortwave radiation change in response to SIC change is more significant in summer months. We found that using annual means without taking into account the seasonal cycle leads to bias both locally and globally;

however, using monthly means also introduces errors as it does not capture the portion of the TOA radiation response that is lagged relative to the surface warming. Therefore, we average to four seasonal-mean Jacobians (DJF/MAM/JJA/SON) to produce all annual-averaged responses.

Lastly, all the patch experiments as well as the two AGCM experiments, the *Historical* run and the $4\times CO_2$ run, do not include changes in any radiative forcing agents, and therefore lack feedbacks associated with land warming in direct response to radiative forcing. Here, the change in feedback arises only from the change in SST/SIC boundary forcing. We note this as a caveat, but it allows us to track the sensitivity of feedbacks to evolving spatial patterns of SSTs.

3. Global response to localized warming

We compare responses to four warming patches within several key regions highlighted in previous studies (e.g., Andrews and Webb 2017; Zhou et al. 2017): the west Pacific, the east Pacific, and high latitudes in the Northern Hemisphere (NH) and the Southern Hemisphere (SH) (Fig. 4). Importantly, SST warming in the western Pacific (a region of tropical ascent) drives strong remote responses on a global scale; while the responses to SST warming in the other three regions are more confined locally. For the west Pacific patch (Fig. 4a), warming is communicated to the upper troposphere, which warms the whole troposphere across all latitudes, causing a large increase in outgoing radiation at the TOA. Furthermore, the patch of warming locally decreases tropospheric stability, measured here as estimated inversion strength (EIS), but increases EIS remotely over tropical marine low clouds regions, yielding an increase in global low cloud cover (LCC) which enhances the global SW reflection (Wood and Bretherton 2006). In contrast, surface warming in the east Pacific patch and high-latitude patches results in atmospheric warming that is trapped within the boundary layer and decreases local EIS and LCC, leading to a weakly positive TOA radiation change that is limited to local scale (Fig. 4 b, c, d). Overall, the global-mean TOA radiation and TAS responses to the west Pacific patch are about an order of magnitude greater than the responses to the three other patches.

The difference between NH and SH polar patches reveals another feature in net TOA radiation and LCC: the SH polar patch has a negative TOA radiation change and a positive LCC change

(Fig. 4d), which is the result of local sea-ice change. The NH polar patch is applied to a region of open water, where surface warming decreases local EIS and local LCC, resulting in a positive TOA radiation change. However, the SH polar patch is located in the region partially covered by sea ice. When sea ice is forced to melt, new open water enhances heat and moisture transport in the boundary layer, and therefore generates positive LCC change, which reflects more TOA radiative fluxes (Wall et al. 2017; Goosse et al. 2018). However, this sea-ice effect shows only a small impact on the global scale.

Next, we show the global-mean response to unit SST warming in each grid box (Fig. 5). The annual-global-mean net TOA radiation change and annual-global-mean TAS change to each grid of SST warming (Fig. 5a and 5b, respectively) are calculated from seasonal Jacobians $\boldsymbol{\mathcal{J}_R}$ and $\boldsymbol{\mathcal{J}_T}$. Dividing the global TOA response by the global TAS response provides a qualitative sense of how the global feedback changes in response to a localized warming in each grid box (Fig. 5c). Consistent with Fig. 4, surface warming in tropical ascent regions has the strongest remote effect, driving large increases in outgoing TOA radiation and thus large negative feedbacks. Surface warming in tropical descent regions drives a relatively weaker increase in outgoing radiation, or even a decrease, thus producing more positive feedback values, consistent with previous studies (e.g., Andrews and Webb 2017; Ceppi and Gregory 2017; Zhou et al. 2017). High-latitude warming plays an important role in global TAS change, but contributes little to global TOA radiation change, leading to feedback values near zero.

We further partition the net TOA radiation response into individual components by use of radiative kernels (Shell et al. 2008) (Fig. 5d – i). The large net negative radiation response to warming in tropical ascent regions arises from Planck radiation, lapse rate (LR), and cloud SW radiation changes. The net positive radiation response to warming in descent regions is dominated by cloud SW radiation changes. The Planck response (Fig. 5d) largely mirrors the response of global TAS to local warming (Fig. 5b), as it must: it is negative in response to warming everywhere but the magnitude is larger in response to warming in the western Pacific as opposed to all other regions. The patterns of LR change (Fig. 5e) and water vapor change (Fig. 5f) are consistent with those proposed by Andrews and Webb (2017) and Ceppi and Gregory (2017). While radiation changes with LR and water vapor partially cancel when summed, the net value here is not zero and instead shows a pattern similar to the LR change (not shown), indicating a stronger radiative response associated with LR changes. The pattern of cloud SW changes (Fig. 5g), which dominates the net TOA radiation pattern, suggests that

LCC plays an important role in changing global TOA radiation. The global surface albedo change (Fig. 5i) is negligible everywhere, arising from the fact that sea-ice albedo changes result in localized TOA radiation changes.

4. Green's function validation

Before moving to the final step of applying the Jacobians to attribute feedback changes to regional warming, we validate the Green's function approach. First, we perform a linearity test by imposing two SST patches in a simulation simultaneously – one in the tropical west Pacific and one in the tropical east Pacific (noted as the *Two-Patch* run, Fig. 6a). The CAM4-produced output in this *Two-Patch* run is then compared to the linear sum of the response to two corresponding single patches (Fig. 6b). We find a remarkable similarity in spatial patterns for all responses of interests with spatial correlations higher than 90%, and nearly-identical global-mean responses (shown in Fig. 6). This test speaks to the strong linearity in the model's responses, supporting the assumption that the response to a large-scale SST pattern can be estimated as the sum of responses to each of the SST forcing point. Additional two-patch tests performed within other regions also exhibit a strong linearity (not shown).

Next, we convolve the SST patterns from the *Historical* run and the $4{\times}CO_2$ run with the Green's function, and compare the reconstructed response with the CAM4-produced response (Fig. 7). For both runs, the Green's function reproduces the inter-annual variability and overall magnitude of global net TOA radiation, TAS, and radiative feedback. We note an offset in global-mean TOA radiation and radiative feedback in the $4{\times}CO_2$ run; we will discuss reasons of this potential nonlinearity in section 6b. Despite this relatively small offset for the $4{\times}CO_2$ simulation, the Green's function reconstruction captures most of the feedback changes seen in both simulations. We interpret these results as a validation of the robustness of the Green's function approach, allowing us to proceed with attributing feedback changes to regional warming patterns.

5. Attributing global feedback changes to regional warming

The selected patches in section 3 (Fig. 4) reveal an important property in the climate system: temperature and radiation changes depend on both local and remote surface warming. In this section, we identify where the changes in TOA radiation and TAS originate using the global-mean net TOA radiation change (ΔR_{global_i}) and global-mean TAS change (ΔT_{global_i}) that are associated with SST and SIC perturbations in any grid box *i* in a particular warming pattern:

$$\Delta R_{global_i} = \frac{\partial R_{global}}{\partial SST_i}\Delta SST_i + \alpha\frac{\partial R^*{}_{global}}{\partial SIC_i}\Delta SIC_i^*, \tag{17}$$

$$\Delta T_{global_i} = \frac{\partial T_{global}}{\partial SST_i}\Delta SST_i + \alpha\frac{\partial T^*{}_{global}}{\partial SIC_i}\Delta SIC_i^*. \tag{18}$$

$\frac{\partial R_{global}}{\partial SST_i}$ and $\frac{\partial T_{global}}{\partial SST_i}$ are global-mean net TOA radiation change and global-mean TAS change to unit SST change in grid box *i* (Fig. 5a and 5b), respectively; ΔSST_i is SST anomaly at grid box *i* in a particular warming pattern; $\frac{\partial R^*{}_{global}}{\partial SIC_i}$ and $\frac{\partial T^*{}_{global}}{\partial SIC_i}$ are global-mean net TOA radiation change and global-mean TAS change to unit SIC change in grid box *i* if *i* is covered by sea ice, and ΔSIC_i^* is SIC anomaly in this warming pattern that is not fully captured by the patch experiments setting (at the rate of -20% per +3K SST change). Since the Jacobians with respect to SIC, $\boldsymbol{\mathcal{J}_R}^*$ and $\boldsymbol{\mathcal{J}_T}^*$ only represents local SIC effect, the second term on the right-hand-side in Eq. (17) and Eq. (18) is close to zero. ΔR_{global_i} and ΔT_{global_i} represent the contribution from local SST change to global averaged change in TOA radiation and TAS, given a specific surface warming pattern.

We first show ΔR_{global_i} and ΔT_{global_i} for the *Historical* run (Fig. 8), using the SST and SIC change averaged over the 1950s and the 2000s, relative to the pre-industrial level (i.e., averaged over year 1850-1890). The most striking finding is that the more negative TOA radiation in the 2000s is predominately due to SST change in tropical ascent regions (Fig. 8d). While many studies (e.g., Andrews and Webb 2017; Zhou et al. 2016) focus on the zonal SST gradient with preferential cooling in the eastern Pacific in this period, our result highlights the role of the western Pacific in driving most of the change in global TOA radiation. This arises for two reasons: (i) stronger surface warming in this region relative to the rest of the world oceans over the recent decades (Fig. 8b); (ii) stronger global radiative response to surface warming from this region driven by the deep convection (Fig. 5a). Overall, comparing the 1950s and the 2000s, the primary change in both global-mean TOA radiation and TAS from the early period to the late period is due to warming in tropical ascent regions.

Next, we show the same analysis for the *4×CO₂* run (Fig. 9), comparing the first 20 years in the simulation to the last 20 years. In this case, although global SSTs evolve toward a pattern with more warming in the eastern Pacific and high latitudes, the western Pacific is still the dominant contribution to the global TOA radiation change, in both the early and late period. However, the evolution of the contribution to global TAS change shows a different behavior: SST warming outside of the deep convective regions, although contributing little in the early period, plays an ever-increasing role in global TAS change in the latter period.

The attribution analysis for the two simulations can be summarized as follows: (i) in both runs, the change in global TOA radiation is dominated by the radiative response to warming in tropical ascent regions; (ii) this does not hold true for TAS, however, which has substantial contributions from all other regions. Based on these findings, we propose a guiding approximation:

$$\lambda(t) \approx \frac{\Delta R_{global\_WP}}{\Delta T_{global\_WP} + \Delta T_{global\_other}}, \tag{19}$$

where ΔR_{global_WP} and ΔT_{global_WP} respectively denote global-mean net TOA radiation change and TAS change that are attributed to surface warming in the warm pool (WP) region, and ΔT_{global_other} denotes global-mean TAS change that is attributed to surface warming in all other oceans outside of the WP. The WP region is defined here as broad deep convective areas in Indo-Pacific Ocean within 30°S - 30°N and 50°E - 160°W (shown as the grey box in Fig. 8 and Fig. 9) capturing the region with the most negative values of ΔR_{global_i} (Fig. 8 and Fig. 9). From this approximation, we can then reformulate the global radiative feedback as

$$\lambda(t) = \frac{\lambda_{WP}}{1 + \gamma(t)}, \tag{20}$$

where $\lambda_{WP} = \Delta R_{global\_WP} / \Delta T_{global\_WP}$ denotes a nominal and constant value of feedback associated with the WP warming, and $\gamma(t)$ is given by

$$\gamma(t) = \frac{\Delta T_{global\_other}}{\Delta T_{global\_WP}}. \tag{21}$$

$\gamma(t)$ is the "warm pool (WP) warming ratio", representing the ratio of the contribution to global TAS change from surface warming in all ocean areas outside of the WP relative to the contribution from surface warming within the WP region.

In this formulation (Eq. 19-21), we first approximate global-mean TOA radiation change to a response to SST change in the WP region alone (Eq. 19); the time-variation of feedback can then be explained by the evolution of γ (Eq. 20), which compares how regional warming affects global TAS change (Eq. 21). When γ decreases with time, meaning that the WP warming contributes more to global-mean TAS change, the strength of net global radiative feedback will be larger, i.e., a more negative value. This is because the surface warming in the WP is communicated to the free troposphere, driving more outgoing radiation to space that efficiently damps the heating, thus leading to a more negative feedback. In contrast, when γ increases with time, meaning that warming outside of the WP features more in global-mean TAS change, then the feedback will be smaller in magnitude, i.e., a less negative value. This is because the local surface warming in tropical descent regions and high latitudes tends to be constrained near the surface, driving much smaller changes in global TOA radiation, and resulting in a less negative feedback.

In Fig. 10, we show the evolution of γ calculated by Eq. (21) for the *Historical* run and the *4×CO₂* run, and compare the evolution of the net feedbacks with the approximated feedbacks calculated by Eq. (19) to test this approximation. In both the historical warming and future warming simulation, the evolution of γ is responsible for the evolution of the strength of the global feedback, and the approximated feedback captures the main trend of the net feedback changes throughout the whole period. The radiation change induced by the east Pacific warming and all other oceans outside of the WP plays a minor role in feedback evolution. This confirms the assumption that surface warming in the WP region controls the change in global TOA radiation, and the evolution of global radiative feedbacks is thus due to the evolution of γ.

In summary, applying the Green's function approach we are able to isolate the effect of regional warming on global TOA radiation, TAS, and feedback changes, respectively, for different time periods. In contrast to previous studies that focus on the tropical east-west SST gradient, our study pinpoints the relative importance of the western Pacific as the dominant driver of changes in global TOA radiation. We also propose that global feedback changes track the ratio of the contribution to global TAS change from regional surface warming in the WP region relative to the contribution from warming in all other regions. For example, the more positive feedback associated with high-latitude warming in the future can be attributed to the increased contribution to global TAS change from surface warming in this region, rather than to a positive change in global TOA radiation due to high-latitude warming as proposed in other studies (e.g., Armour et al. 2013; Li et al. 2013).

6. Discussion

The major caveats to the above results are considered in this section: the sensitivity of the results to the strength of cloud feedback and cloud parameterization in the AGCM we used, and the potential reasons for the noticeable nonlinearity in radiative response seen in the *4×CO₂* run (Fig. 7 d, f).

a. Comparison with CAM5

One limitation of our results is the use of CAM4, which is known to lack an accurate representation of LCC sensitivity to local SST changes, and therefore potentially leads to less positive cloud feedback associated with warming in tropical descent regions (e.g., Gettelman et al. 2012; Park et al. 2014). We thus compare the CAM4 Green's function to that of CAM5 (using output from the simulations of Zhou et al. 2017), which has an improved capacity to simulate LCC response to both local SST change and tropospheric stability change (Park et al. 2014). Fig. 11 shows the comparison of global-mean cloud radiative effect (CRE) and global-mean net TOA radiation to each grid of unit SST warming. (CRE is defined as the difference between net TOA radiation and clear-sky net TOA radiation). The patterns are consistent between the two models, although CAM4 has greater CRE and net TOA radiation response to SST warming in the warm pool region.

To test the robustness of our results considering the processes that contribute to the time-variation of global feedbacks, we repeat the calculations of Eq. (19) but using the CAM5 Green's function. We find that feedback approximation, using only the global-mean TOA radiative response to SST change in the WP region, still captures most of the temporal variations in the net feedback in both the *Historical* run (Fig. 11e) and the *4×CO₂* run (Fig. 11f). This agreement between CAM4 and CAM5 suggest that the key result of this study – that warming in the western tropical Pacific dominates global feedback changes for historical and future warming – is robust across models with different cloud parameterizations.

b. Nonlinearity in the 4×CO₂ simulation

In section 4, we found that the global-mean TOA radiation, and thus radiative feedback, reconstructed from the Green's function were offset from those in the *4×CO₂* run (Fig. 7 d, f), suggesting a nonlinear behavior. This offset appears in the first few decades, and then remains relatively constant over the rest of the simulation. We propose three hypotheses that could account for this nonlinearity.

The first hypothesis is that there may be a nonlinearity in global-mean TOA radiation change that is associated with global-mean temperature change (e.g., Bloch-Johnson et al. 2015). This would result in a residual between the Green's function reconstruction and model output, hereafter noted as ΔR_{res}, that should scale as a quadratic function of global-mean temperature: $b\Delta T^2$,where b has unit of $Wm^{-2}K^{-2}$ (Bloch-Johnson et al. 2015). That is, the feedback ($\Delta R/\Delta T$), instead of being constant, may increase with global-mean temperature (Meraner et al. 2013; Block and Mauritsen 2013). If this holds, we would expect $\Delta R_{res} = b\Delta T^2$, or $\Delta R_{res}/\Delta T = b\Delta T$. Comparing ΔR_{res} from the *4×CO₂* simulation to that expected based on b values found in other model simulations (Meraner et al. 2013; Roe and Armour, 2011) shows that this nonlinearity does not appear to explain the residual (Fig. 12). Instead, ΔR_{res} appears to show three separate regimes as time evolves: the first 1-2 years, the first few decades, and the longer time scale in the rest of 150 years. This seems more consistent with the three modes of evolving warming patterns proposed by Proistosescu and Huybers (2017). Only the second mode shows a nonlinear-like behavior, yet the best-fitting value of b (approximately 0.17 $Wm^{-2}K^{-2}$) is well above the maximum value (0.06 $Wm^{-2}K^{-2}$) found in previous studies (Roe and Armour 2011). Moreover, after the first few decades, ΔR_{res} no longer fits the expected nonlinear relationship.

While the global-mean temperature nonlinearity does not explain the residual, it is possible that there could be a nonlinearity associated with local temperature change. That is, the error in global-mean TOA radiation estimate could arise from the local SST changes in the simulation being substantially larger than the SST anomalies we imposed to derive the Green's function. To test this possibility, we perform an additional 30 year-long simulation, in which the SST/SIC anomalies have the same spatial pattern as in the last 30 years of the *4×CO₂* run, but the magnitude of the anomalies is reduced by 1/6 at all locations such that the global-mean SSTs are comparable to that of the last 30 years of the *Historical* run (hereafter, the *ReducedSST* run). In this simulation (see Fig. 7, blue lines), the offset between the CAM4-produced response (Fig. 7d, blue solid line) and Green's function reconstructed response (Fig. 7d, blue dashed line) still remains, suggesting that the magnitude of local temperature is not the reason leading to the error.

Therefore, we hypothesize that the nonlinearity in global-mean radiation may be arising from the peculiar spatial pattern of SST/SIC changes in the *4×CO₂* simulation. For example, increasing CO_2 causes a zonal shift in the locations of tropical convection associated with an El Niño-like warming pattern. However, we have not seen such a nonlinearity in additional simulations similar to those in section 4, e.g., two adjacent patches in the tropical eastern Pacific. Although a detailed mechanism still remains unclear, we postulate that the particular warming pattern in this simulation may be responsible for the nonlinearity, which suggests the possibility of a new type of nonlinearity that has not been previously documented.

7. Conclusion

Here we have examined the historical and future evolution of global radiative feedbacks within two AGCM simulations. Feedbacks trend toward more negative values over time for historical warming, yet trend toward more positive values over time under 4×CO_2. To quantify the impact of regional SST anomalies on global TOA radiation and TAS, we derived a Green's function from a suit of patch simulations within CAM4, permitting the attribution of feedback changes to surface warming in each region.

The results first highlight the radiative response to surface warming in tropical ascent regions as the dominant control of global TOA radiation change both in the past and in the future. We propose that, to a good approximation, global radiative feedback changes track the "warm pool warming ratio" (γ), defined here as the ratio of contribution to global TAS change from surface warming in the regions outside of the WP relative to the contribution from warming in the WP region alone. We found that historical TAS changes from the 1950s to 2000s are preferentially attributed to SST changes in the warm pool, i.e., γ is small over recent decades. This surface warming pattern yields a strong global outgoing radiative response at TOA that can efficiently damp the surface heating, therefore producing a very negative global feedback. The projected future change in global TAS, on the other hand, features more warming in the tropical descent regions and in high latitudes than in the tropical ascent regions (the WP), i.e., γ increases by time. Surface warming from regions outside of deep convective regions yields locally amplified warming effects but limited global TOA radiation changes, thus leading to a less-negative global feedback in the projected (future) climate.

Comparing our results from CAM4 to those based on the CAM5 Green's function of Zhou et al. (2017) shows that while the cloud radiative response is somewhat different between the two models, there is consistency between CAM4 and CAM5 regarding the regions of importance for feedback changes. An expanded inter-model comparison using the Green's function approach from multiple GCMs would be valuable. We also examined potential reasons for the nonlinearity seen in the *4×CO₂* simulation. The specific mechanism is not clearly understood, but we propose that it might arise from the particular spatial pattern of SSTs in this simulation, rather than arising from nonlinearities associated with global-mean or local temperature changes, as proposed by previous studies.

This study highlights the importance of warm pool warming relative to the rest of the world oceans for the evolution of global radiative feedbacks, both historically and in the future under CO_2 forcing. A key question is thus whether the western Pacific will continue to warm quickly relative to the rest of the world oceans, as we have seen in observations to date, or whether it will warm by relatively less in the future, as GCMs predict. These results suggest that only in the case that the western Pacific warming keeps warming at a greater place than the rest of the global oceans can we expect ICS to remain as low as that derived from recent energy budget constraints (e.g., Otto et al. 2013; Lewis and Curry 2015; 2018; Armour 2017; Knutti et al. 2017). If GCMs are accurate in their projection that the western Pacific warming will not keep pace with the eastern Pacific and high latitude warming, then we can expect a less negative feedback, and a higher value of ICS, in the future.

Acknowledgements

YD and KCA were supported by National Science Foundation grant AGS-1752796, CP was supported by JISAO postdoctoral fellowship, and DSB was supported by the Tamaki Foundation. We thank C. Zhou, M. Zelinka, S. Klein, R.J. Wills and A.L.S. Swann for insightful discussions. We acknowledge C. Zhou for sharing data associated with the CAM5 Green's functions, and M.M. Laguë, M.F. Stuecker, and C.M. Bitz, for assisting with the CAM4 simulations.

Reference

Andrews, T., Gregory, J. M., Paynter, D., Silvers, L. G., Zhou, C., Mauritsen, T., … Titchner, H. (2018). Accounting for Changing Temperature Patterns Increases Historical Estimates of Climate Sensitivity. *Geophysical Research Letters*, *45*(16), 8490–8499. https://doi.org/10.1029/2018GL078887

Andrews, T., Gregory, J. M., & Webb, M. J. (2015). The dependence of radiative forcing and feedback on evolving patterns of surface temperature change in climate models. *Journal of Climate*, *28*(4), 1630–1648. https://doi.org/10.1175/JCLI-D-14-00545.1

Andrews, T., Gregory, J. M., Webb, M. J., & Taylor, K. E. (2012). Forcing, feedbacks and climate sensitivity in CMIP5 coupled atmosphere-ocean climate models. *Geophysical Research Letters*, *39*(9), 1–7. https://doi.org/10.1029/2012GL051607

Andrews, T., & Webb, M. J. (2018). The dependence of global cloud and lapse rate feedbacks on the spatial structure of tropical pacific warming. *Journal of Climate*, *31*(2), 641–654. https://doi.org/10.1175/JCLI-D-17-0087.1

Armour, K. C. (2016). Projection and prediction: Climate sensitivity on the rise. *Nature Climate Change*, *6*(10), 896–897. https://doi.org/10.1038/nclimate3079

Armour, K. C. (2017). Energy budget constraints on climate sensitivity in light of inconstant climate feedbacks. *Nature Climate Change*, *7*(5), 331–335. https://doi.org/10.1038/nclimate3278

Armour, K. C., Bitz, C. M., & Roe, G. H. (2013). Time-Varying Climate Sensitivity from Regional Feedbacks. *Journal of Climate*, *26*(13), 4518–4534. https://doi.org/10.1175/JCLI-D-12-00544.1

Barsugli, J. J., & Sardeshmukh, P. D. (2002). Global atmospheric sensitivity to tropical SST anomalies throughout the Indo-Pacific basin. *Journal of Climate*, *15*(23), 3427–3442. https://doi.org/10.1175/1520-0442(2002)015<3427:GASTTS>2.0.CO;2

Bloch-Johnson, J., Pierrehumbert, R. T., & Abbot, D. S. (2015). Feedback temperature dependence determines the risk of high warming. *Geophysical Research Letters*, *42*(12), 4973–4980. https://doi.org/10.1002/2015GL064240

Block, K., & Mauritsen, T. (2013). Forcing and feedback in the MPI-ESM-LR coupled model under abruptly quadrupled CO $_2$. *Journal of Advances in Modeling Earth Systems*, *5*(4), 676–691. https://doi.org/10.1002/jame.20041

Ceppi, P., & Gregory, J. M. (2017). Relationship of tropospheric stability to climate sensitivity and Earth’s observed radiation budget. *Proceedings of the National Academy of Sciences*, 201714308. https://doi.org/10.1073/pnas.1714308114

Feldl, N., & Roe, G. H. (2013). The nonlinear and nonlocal nature of climate feedbacks. *Journal of Climate*, *26*(21), 8289–8304. https://doi.org/10.1175/JCLI-D-12-00631.1

Gettelman, A., Kay, J. E., & Shell, K. M. (2012). The evolution of climate sensitivity and climate feedbacks in the community atmosphere model. *Journal of Climate*, *25*(5), 1453–1469. https://doi.org/10.1175/JCLI-D-11-00197.1

Goosse, H., Kay, J. E., Armour, K. C., Bodas-Salcedo, A., Chepfer, H., Docquier, D., … Vancoppenolle, M. (2018). Quantifying climate feedbacks in polar regions. *Nature Communications*, *9*(1). https://doi.org/10.1038/s41467-018-04173-0

Gregory, J. M., & Andrews, T. (2016). Variation in climate sensitivity and feedback parameters during the historical period. *Geophysical Research Letters*, *43*(8), 3911–3920. https://doi.org/10.1002/2016GL068406

Gregory, J. M., Ingram, W. J., Palmer, M. A., Jones, G. S., Stott, P. A., Thorpe, R. B., … Williams, K. D. (2004). A new method for diagnosing radiative forcing and climate sensitivity. *Geophysical Research Letters*, *31*(3), 2–5. https://doi.org/10.1029/2003GL018747

Hurrell, J. W., Hack, J. J., Shea, D., Caron, J. M., & Rosinski, J. (2008). A new sea surface temperature and sea ice boundary dataset for the community atmosphere model. *Journal of Climate*. https://doi.org/10.1175/2008JCLI2292.1

Knutti, R., Rugenstein, M. A. A., & Hegerl, G. C. (2017). Beyond equilibrium climate sensitivity. *Nature Geoscience*, *10*(10), 727–736. https://doi.org/10.1038/NGEO3017

Lewis, N., & Curry, J. A. (2015). The implications for climate sensitivity of AR5 forcing and heat uptake estimates. *Climate Dynamics*, *45*(3–4), 1009–1023. https://doi.org/10.1007/s00382-014-2342-y

Lewis, N., & Curry, J. (2018). The impact of recent forcing and ocean heat uptake data on estimates of climate sensitivity. *Journal of Climate*, *31*(15), 6051–6071. https://doi.org/10.1175/JCLI-D-17-0667.1

Li, C., von Storch, J. S., & Marotzke, J. (2013). Deep-ocean heat uptake and equilibrium climate response. *Climate Dynamics*, *40*(5–6), 1071–1086. https://doi.org/10.1007/s00382-012-1350-z

Marvel, K., Pincus, R., Schmidt, G. A., & Miller, R. L. (2018). Internal Variability and Disequilibrium Confound Estimates of Climate Sensitivity From Observations. *Geophysical Research Letters*, *45*(3), 1595–1601. https://doi.org/10.1002/2017GL076468

Mauritsen, T. (2016). Global warming: Clouds cooled the Earth. *Nature Geoscience*, *9*(12), 865–867. https://doi.org/10.1038/ngeo2838

Meraner, K., Mauritsen, T., & Voigt, A. (2013). Robust increase in equilibrium climate sensitivity under global warming. *Geophysical Research Letters*, *40*(22), 5944–5948. https://doi.org/10.1002/2013GL058118

Murphy, J. M. (1995). Transient response of the Hadley Centre coupled ocean-atmosphere model to increasing carbon dioxide. Part III: analysis of global- mean response using simple models. *Journal of Climate*. https://doi.org/10.1175/1520-0442(1995)008<0496:TROTHC>2.0.CO;2

Neale, R. B., Conley, A. J., Lauritzen, P. H., Williamson, D. L., Rasch, P. J., Vavrus, S. J., … Lin, S. (2010). Description of the NCAR Community Atmosphere Model (CAM 4.0), (April). [Available online at http://www.cesm.ucar.edu/models/ccsm4.0/cam/docs/description/cam4_desc.pdf.]

Neale, R. B., Gettelman, A., Park, S., Chen, C., Lauritzen, P. H., Williamson, D. L., … Taylor, M. A. (2012). Description of the NCAR Community Atmosphere Model (CAM 5.0). NCAR Technical Notes. *NCAR Tech. Note NCAR/TN-486+ STR*, (November), 214. [Available online at http://www.cesm.ucar.edu/models/cesm1.0/cam/docs/description/cam5_desc.pdf.]

Otto, A., Otto, F. E. L., Boucher, O., Church, J., Hegerl, G., Forster, P. M., … Allen, M. R. (2013). Energy budget constraints on climate response. *Nature Geoscience*, *6*(6), 415–416. https://doi.org/10.1038/ngeo1836

Park, S., Bretherton, C. S., & Rasch, P. J. (2014). Integrating cloud processes in the Community Atmosphere Model, version 5. *Journal of Climate*, *27*(18), 6821–6856. https://doi.org/10.1175/JCLI-D-14-00087.1

Proistosescu, C., & Huybers, P. J. (2017). Slow climate mode reconciles historical and model-based estimates of climate sensitivity. *Science Advances*, *3*(7), 1–7. https://doi.org/10.1126/sciadv.1602821

Roe, G. H., & Armour, K. C. (2011). How sensitive is climate sensitivity? *Geophysical Research Letters*, *38*(14), 1–5. https://doi.org/10.1029/2011GL047913

Rose, B. E. J., Armour, K. C., Battisti, D. S., Feldl, N., & Koll, D. D. B. (2014). The dependence of transient climate sensitivity and radiative feedbacks on the spatial pattern of ocean heat uptake. *Geophysical Research Letters*, *41*(3), 1071–1078. https://doi.org/10.1002/2013GL058955

Rose, B. E. J., & Rayborn, L. (2016). The Effects of Ocean Heat Uptake on Transient Climate Sensitivity. *Current Climate Change Reports*, *2*(4), 190–201. https://doi.org/10.1007/s40641-016-0048-4

Senior, C. A., & Mitchell, J. F. B. (2000). The time-dependence of climate sensitivity. *Geophysical Research Letters*, *27*(17), 2685–2688. https://doi.org/10.1029/2000GL011373

Shell, K. M., Kiehl, J. T., & Shields, C. A. (2008). Using the radiative kernel technique to calculate climate feedbacks in NCAR's Community Atmospheric Model. *Journal of Climate*, *21*(10), 2269–2282. https://doi.org/10.1175/2007JCLI2044.1

Silvers, L. G., Paynter, D., & Zhao, M. (2018). The Diversity of Cloud Responses to Twentieth Century Sea Surface Temperatures. *Geophysical Research Letters*, *45*(1), 391–400. https://doi.org/10.1002/2017GL075583

Stevens, B., Sherwood, S. C., Bony, S., & Webb, M. J. (2016). Prospects for narrowing bounds on Earth's equilibrium climate sensitivity. *Earth's Future*, *4*(11), 512–522. https://doi.org/10.1002/2016EF000376

Wall, C. J., Kohyama, T., & Hartmann, D. L. (2017). Low-cloud, boundary layer, and sea ice interactions over the Southern Ocean during winter. *Journal of Climate*, *30*(13), 4857–4871. https://doi.org/10.1175/JCLI-D-16-0483.1

Williams, K. D., Ingram, W. J., & Gregory, J. M. (2008). Time variation of effective climate sensitivity in GCMs. *Journal of Climate*, *21*(19), 5076–5090. https://doi.org/10.1175/2008JCLI2371.1

Winton, M., Takahashi, K., & Held, I. M. (2010). Importance of Ocean Heat Uptake Efficacy to Transient Climate Change. *Journal of Climate*, *23*(9), 2333–2344. https://doi.org/10.1175/2009JCLI3139.1

Wood, R., & Bretherton, C. S. (2006). On the relationship between stratiform low cloud cover and lower-tropospheric stability. *Journal of Climate*, *19*(24), 6425–6432. https://doi.org/10.1175/JCLI3988.1

Zhou, C., Zelinka, M. D., & Klein, S. A. (2016). Impact of decadal cloud variations on the Earth's energy budget. *Nature Geoscience*, *9*(12), 871–874. https://doi.org/10.1038/ngeo2828

Zhou, C., Zelinka, M. D., & Klein, S. A. (2017). Analyzing the dependence of global cloud feedback on the spatial pattern of sea surface temperature change with a Green's function approach. *Journal of Advances in Modeling Earth Systems*, *9*(5), 2174–2189. https://doi.org/10.1002/2017MS001096

Table 1. List of experiments performed in this study.

Experiments	**Running time**	**SST/SIC input**	**Description of anomaly defined in this study**
Control	45 years	Monthly-varying observed climatology at the present-day level (averaged over years 1982-2001), from CAM4 model defaults (available at http://www.cesm.ucar.edu/models/cesm1.2/cam/docs/ug5_3/ch03.html)	
Patch Simulations	40 years	Each with a patch of warm SST anomaly and/or SIC anomaly added to the monthly-varying observed climatology used in the *Control* run	The model outputs averaged over the last 39 years relative to the *Control* run's outputs averaged over the entire 45 years.
Historical	165 years (year 1850-2014)	Monthly-varying observed historical SST/SIC (Hurrel et al. 2008) (The CAM4 default time series data is available at http://www.cesm.ucar.edu/models/cesm1.2/cam/docs/ug5_3/ch03.html)	The model outputs spanning over years 1900-2014 relative to the outputs averaged over years 1850-1890 in the same simulation
4×CO₂	150 years	Monthly SST/SIC anomalies from CCSM4 Abrupt4×CO_2 experiment relative to its piControl experiment in CMIP5, added to the monthly-varying observed climatology (used in the *Control* run)	The model outputs spanning over the entire 150 years relative to the *Control* run's outputs averaged over the entire 45 years.
ReducedSST	30 years	As same as the last 30 years of the *4×CO₂* run, except the global-mean magnitude is reduced to be comparable to that of the last 30 years of the *Historical* run	The model outputs spanning over the entire 30 years relative to the *Control* run's outputs averaged over the entire 45 years.

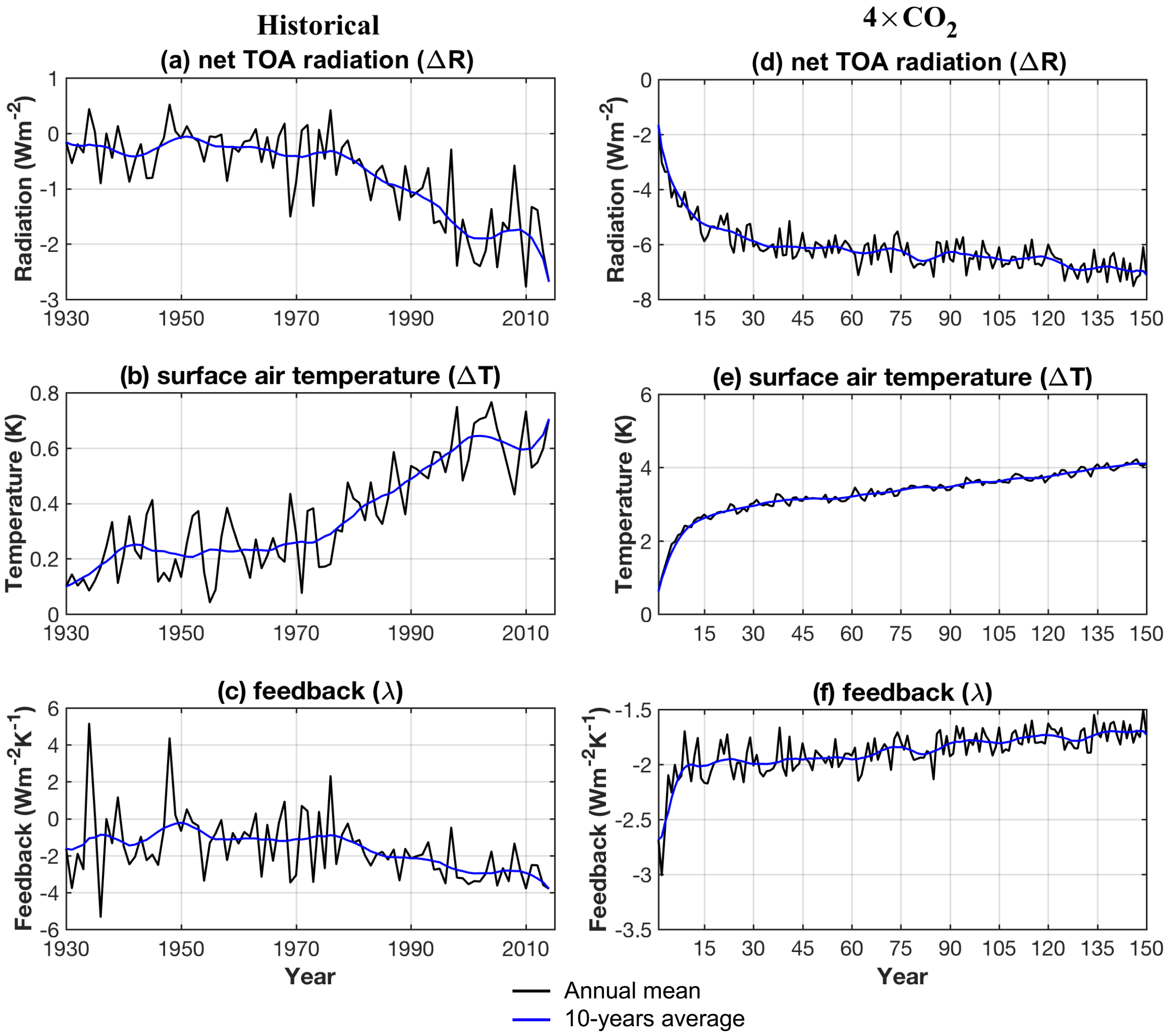

Figure 1: Evolution of global-mean response of (a, d) net TOA radiation (Wm^{-2}), (b, e) near-surface air temperature (K) and (c, f) global feedback (Wm^{-2}K^{-1}) from (left column) the *Historical* run and (right column) the *4×CO$_2$* run. The black lines denote annual mean values, and the blue lines denote 10-years running averages.

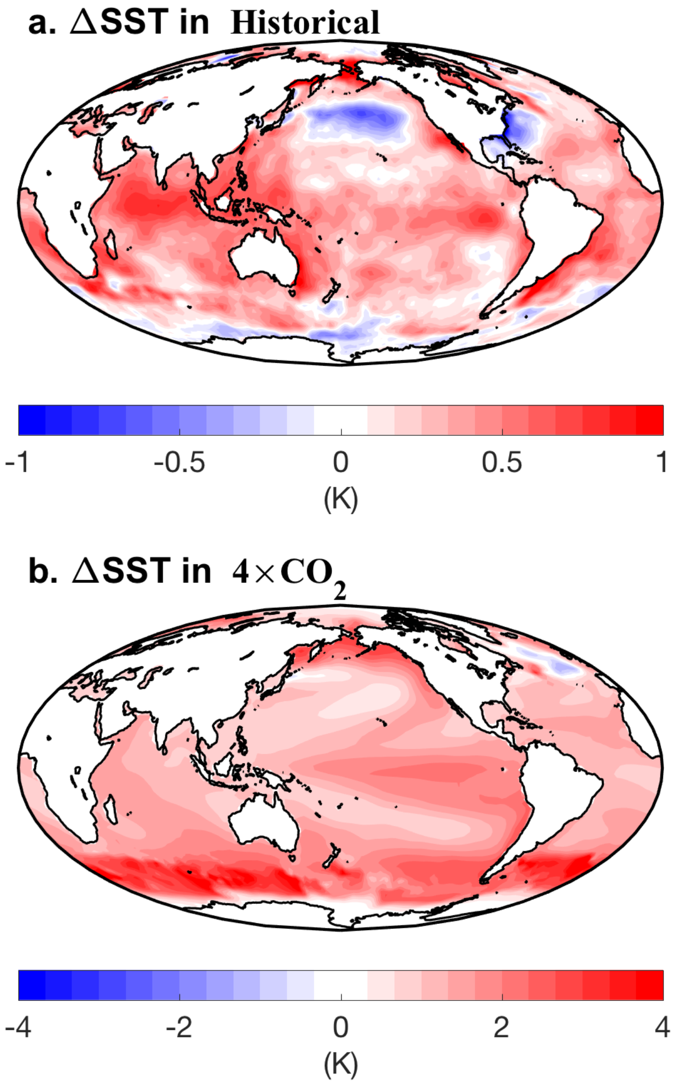

Figure 2: The pattern of SST changes (K) between the late period and the early period, (a) in the *Historical* run (SSTs averaged over years 1996-2005 minus those over years 1956-1965); and (b) in the *4×CO*$_2$ run (SSTs averaged over last 20 years minus those over the first 20 years). Note the color scales in (a) and (b) are different.

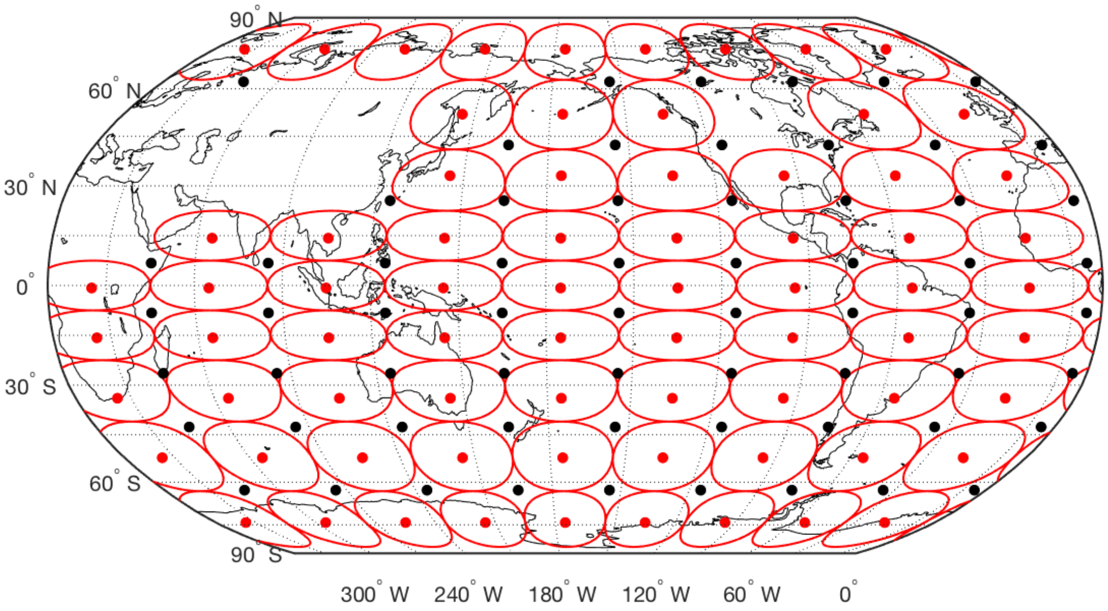

Figure 3: Geographic location of SST patches. Black and red dots denote the center of all patches. The contour denoting the half-amplitude (i.e., 1.5 K for polar patches and 0.75 K for other patches) of each of the red patches is shown, demarking approximately half the size of the patch. The half-amplitude contour for the patches labeled by the black dots are not shown.

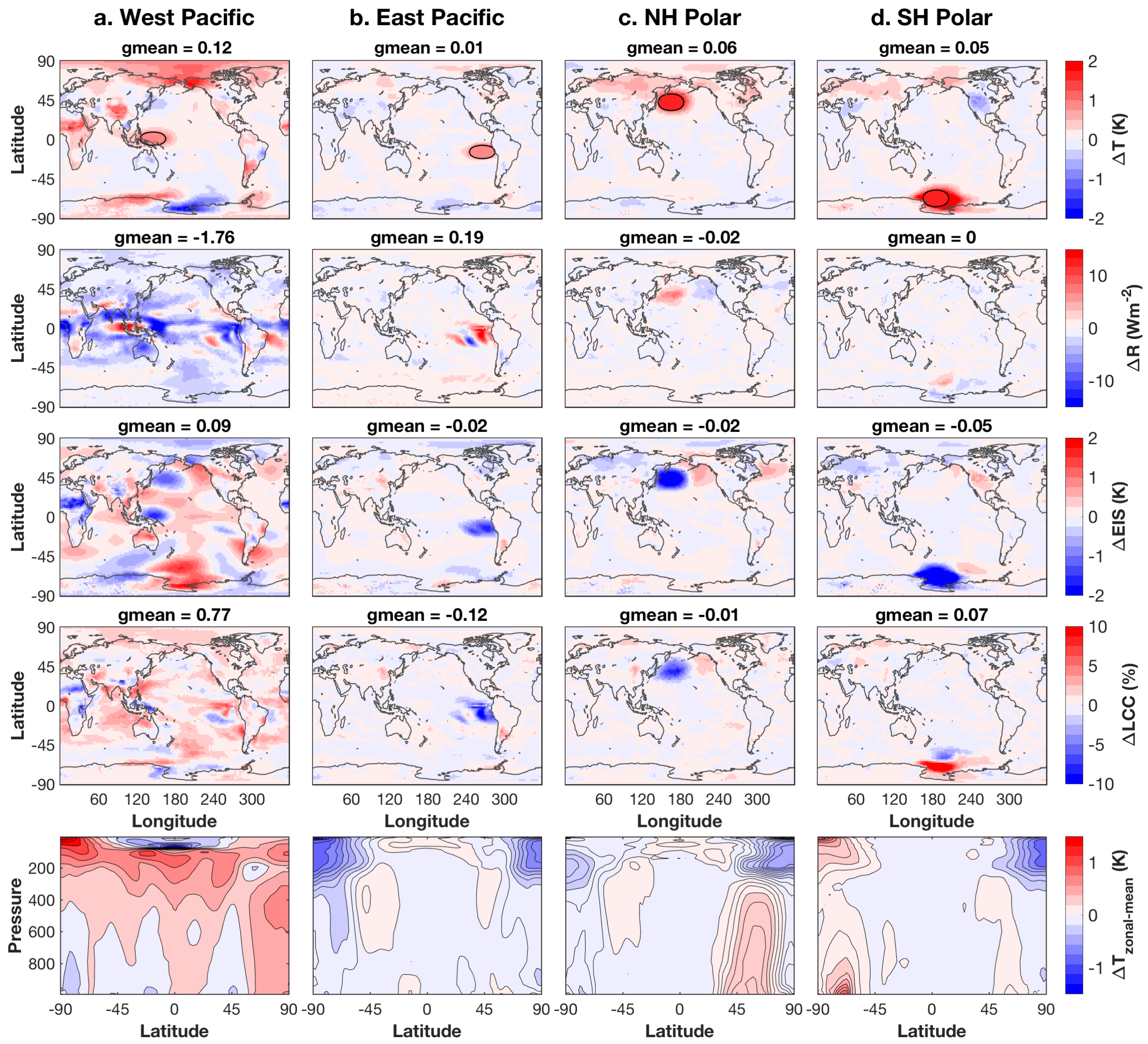

Figure 4: Response to selected SST patches. The patches are identified by the black contour (half-amplitude contour) in the panels in the top row, imposed in (a) the tropical west Pacific, (b) the tropical east Pacific, (c) the Northern Hemisphere high latitude, and (d) the Southern Hemisphere high latitude. From top to bottom: changes in near-surface air temperature ΔT (K), net TOA radiation ΔR (Wm^{-2}), estimated inversion strength ΔEIS (K), low cloud cover ΔLCC (%) and zonal-mean temperature $\Delta T_{zonal\text{-}mean}$ (K). Shown in each panel is the anomalies from each experiment averaged over the last 39 years relative to the *Control* run. The area-weighted global mean of each response is shown at the top of each plot, except for the zonal mean temperature change $\Delta T_{zonal\text{-}mean}$ (bottom row). Note that the amplitude of SST anomalies imposed in polar patches (c, d) is as twice as that imposed in the tropical patches (a, b).

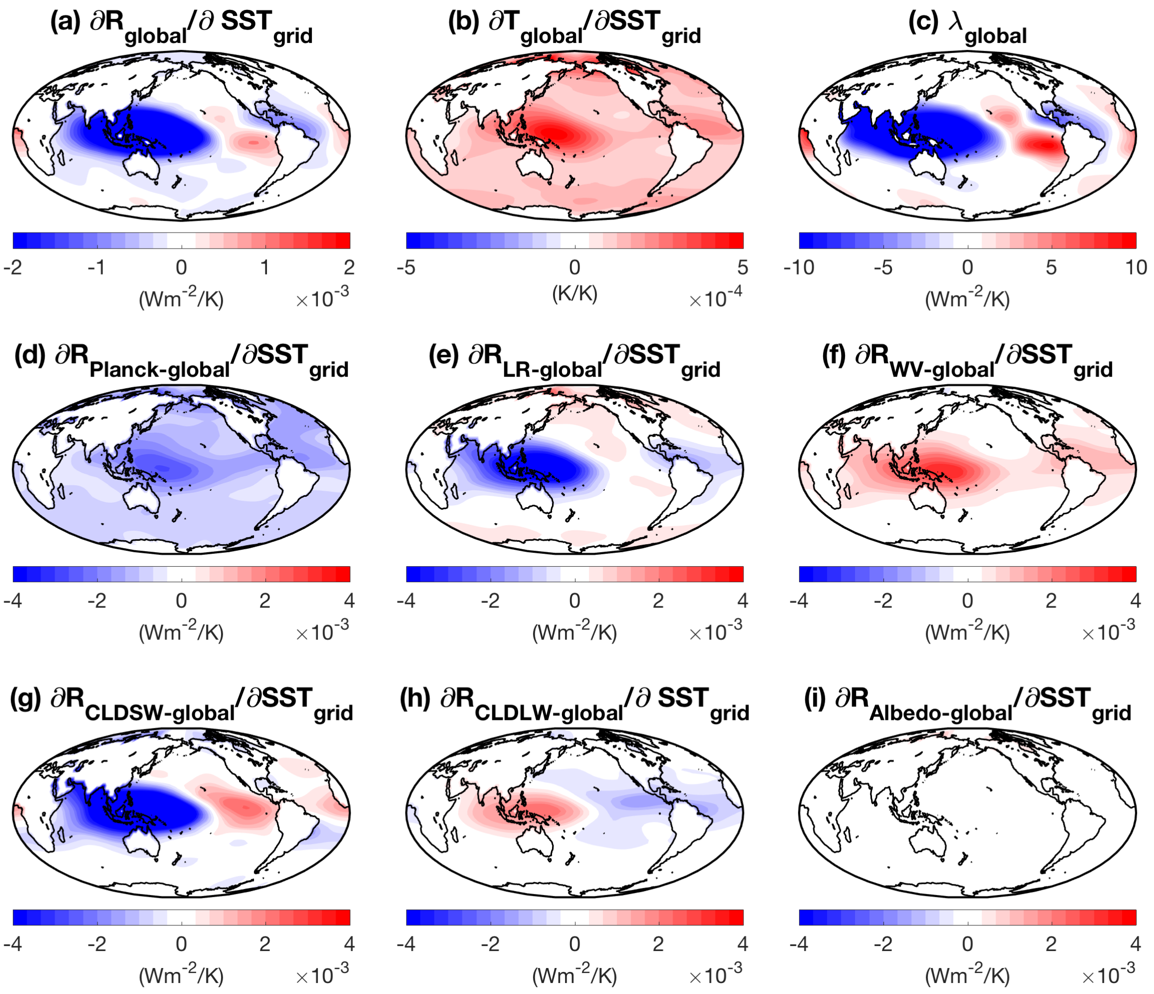

Figure 5: Response of annual and global-mean of (a) net TOA radiation, (b) near-surface air temperature, and (c) feedback to unit SST warming in each grid box. The units are Wm^{-2}/K, K/K, Wm^{-2}/K, respectively. Panel (d) - (i) are individual components of global-mean TOA radiation change shown in (a) decomposed using radiative kernels into contributions due to (d) Planck, (e) lapse rate, (f) water vapor, (g) cloud SW radiation, (h) cloud LW radiation, and (i) albedo changes. The units for panel (d) - (i) are the same as the panel (a), Wm^{-2}/K.

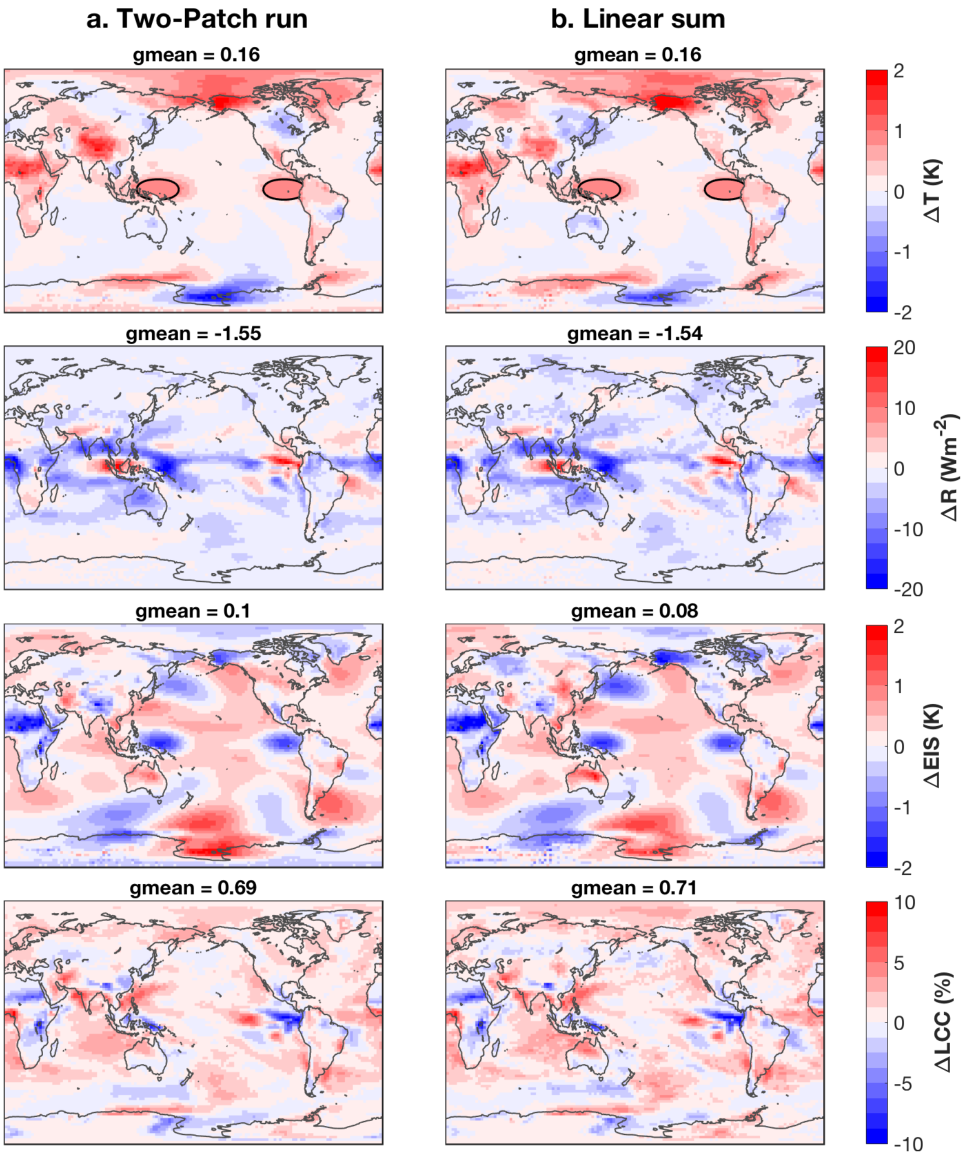

Figure 6: Linearity test with two warming patches in the tropics. The left column (a) shows response from the *Two-Patch* simulation, in which two warming patches are imposed simultaneously: one in the tropical west Pacific, and one in the tropical east Pacific (the patches are identified by the black contour in the panels in the top row). The right column (b) shows the linear sum of responses from two individual simulations, each with a single patch of SST anomalies. Shown in each panel is the anomalies from each experiment averaged over the last 39 years relative to the *Control* run. From top to bottom: near-surface air temperature ΔT (K), net TOA radiation ΔR (Wm^{-2}), estimated inversion strength ΔEIS (K), and low cloud cover ΔLCC (%).

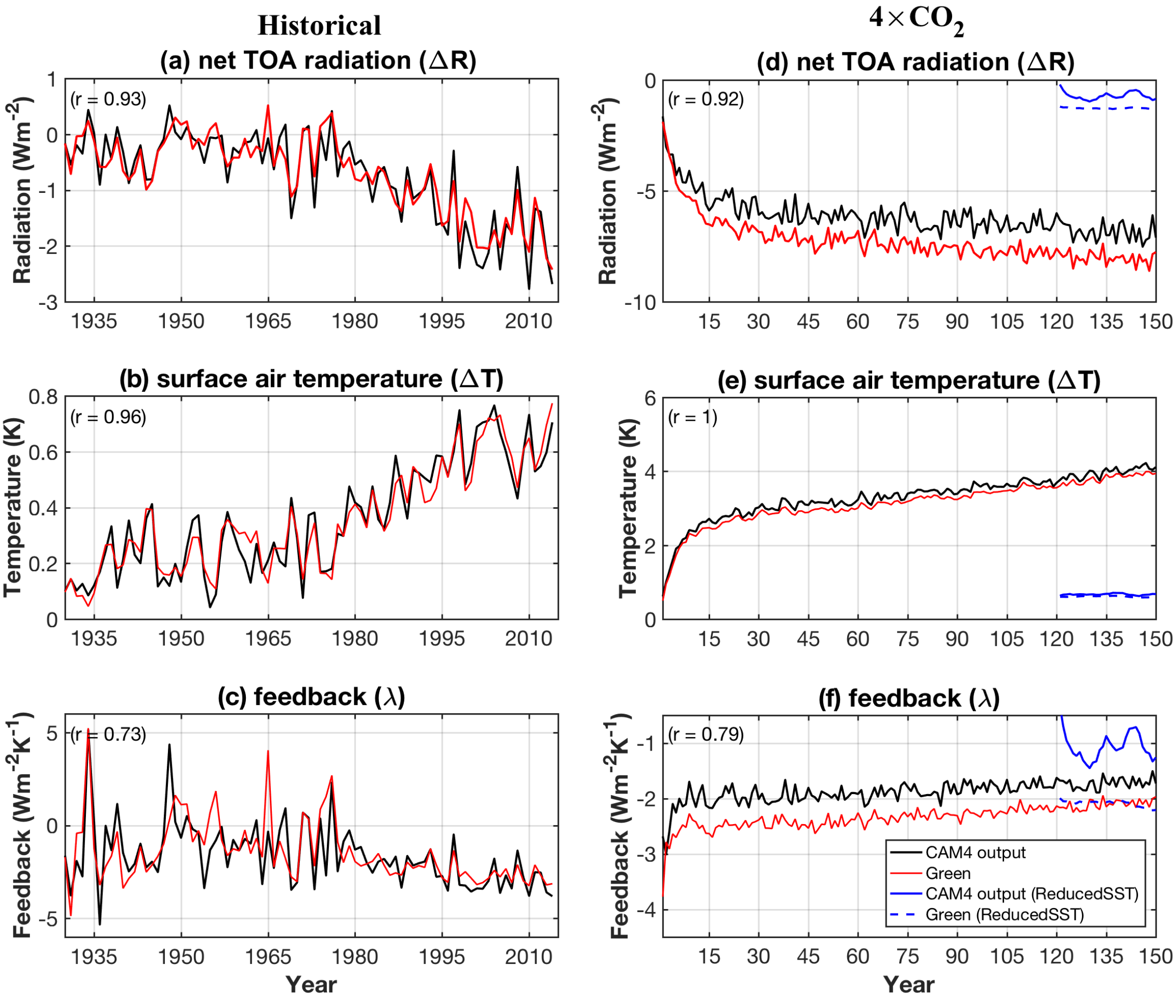

Figure 7: Comparison of the response from CAM4 simulations and the response from the Green's function. The left column shows results for the *Historical* run, the right column shows results for the *4×CO₂* run. From top to bottom: net TOA radiation (Wm^{-2}), near-surface air temperature (K), and global feedback (Wm^{-2} K^{-1}). The black solid lines denote the response from the CAM4 model, the red solid lines denote the response from the Green's function reconstruction. The blue lines denote the response from the 30-years *ReducedSST* run, in which SST/SIC keeps the same pattern as the *4×CO₂* run, but the magnitude of global-mean SST/SIC is reduced by 1/6 to be same as the last 30 years of the *Historical* run. The solid blue line denotes the response from the model, and the dashed blue line denotes the response from the Green's function. (see Table 1 and section 6b for more details.) All the blue lines are running 10 years averages; the black and red lines are annual averages.

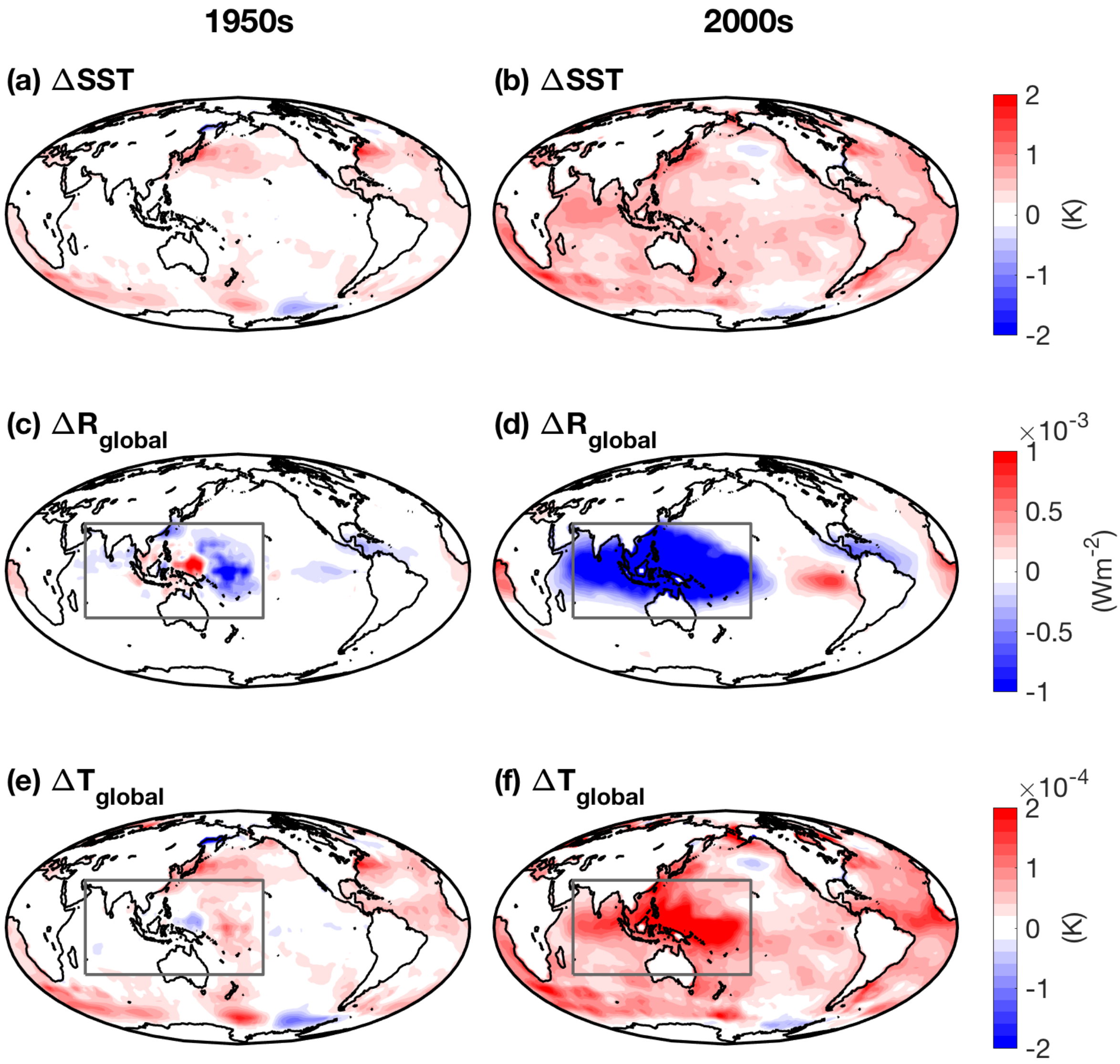

Figure 8: Global-mean response to each grid box of actual SST change in the *Historical* warming pattern. The left column is the averaged response over the 1950s, the right column is the averaged response over the 2000s. (a) and (b) are the SST changes (K) relative to the pre-industrial level (i.e., values averaged over years 1850-1890). (c) and (d) denote the global-mean net TOA radiation response attributed to each grid of SST change (ΔR_{global_i}, unit of Wm^{-2}). (e) and (f) denote the global-mean surface air temperature change attributed to each grid of SST change (ΔT_{global_i}, unit of K). The grey box indicates the area defined as the warm pool in Eq. (19) - Eq. (21) in section 5.

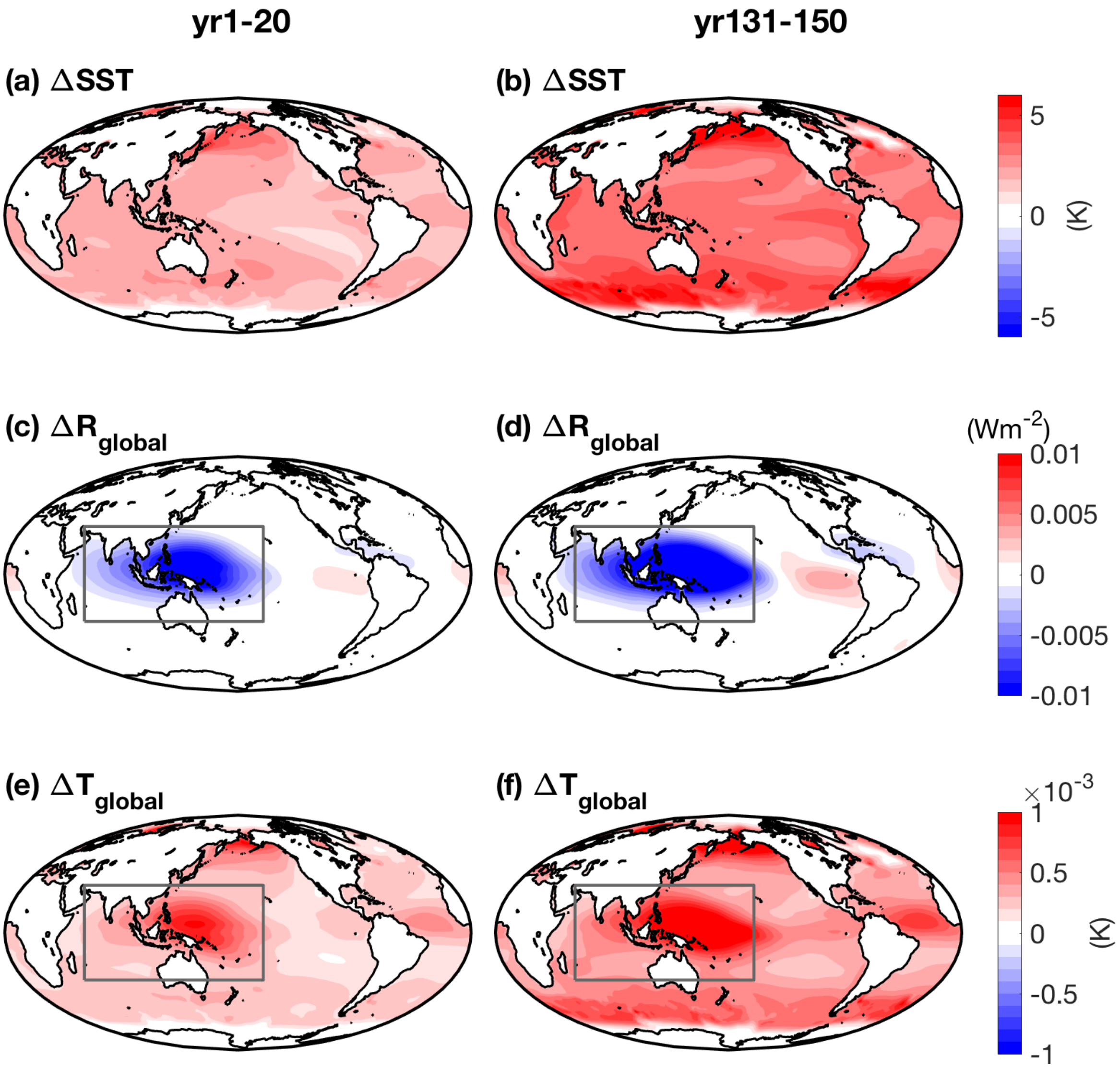

Figure 9: Same as Fig. 8, expect for the *4×CO₂* run. The responses shown are taken as the anomalies relative to the *Control* run. The left column is averaged response over the first 20 years, the right column is averaged response over the last 20 years.

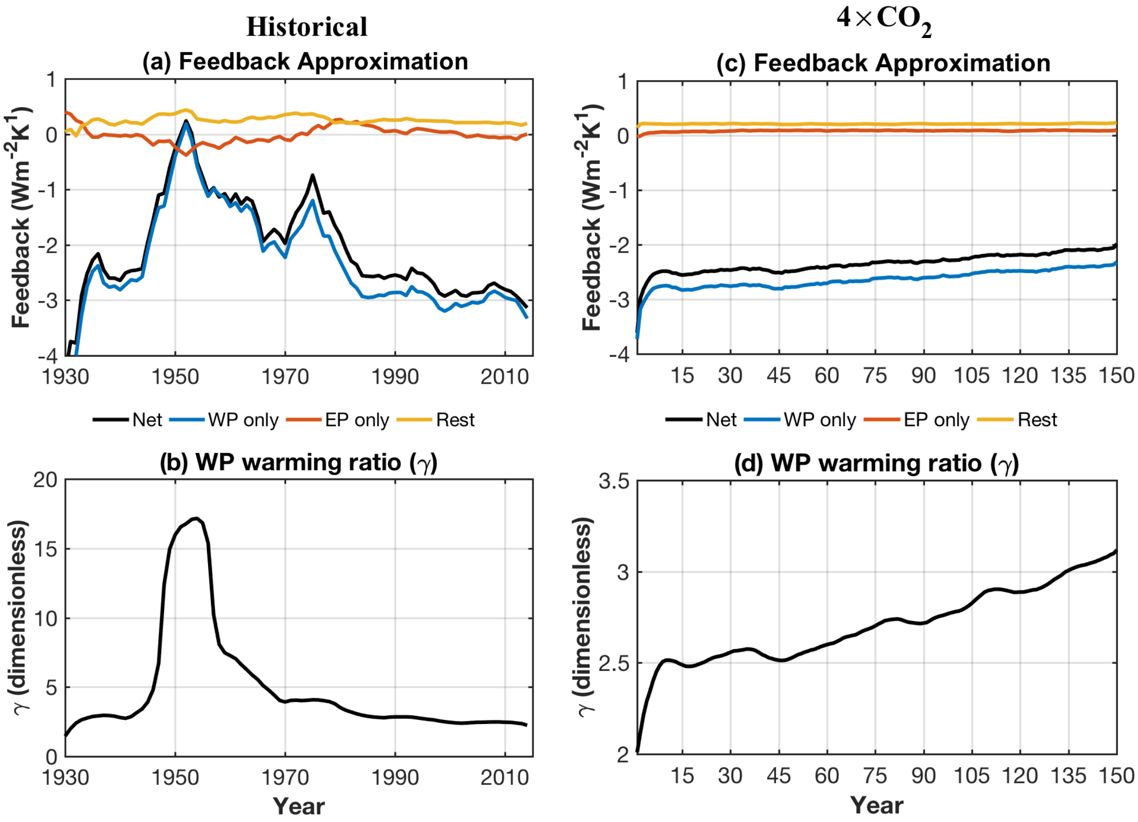

Figure 10: Evolution of radiative feedbacks estimated from the Green's function (a, c) and WP warming ratio γ (b, d), for the *Historical* run (left column) and for the *4×CO₂* run. In panel (a) and (c), the black line ("Net") denotes net feedback, the blue line ("WP only") denotes the approximated feedback calculated by Eq. (19), i.e., the global-mean radiation change is approximated to the radiative response to the warm pool warming alone. The red line ("EP only") shows the estimated feedback using the radiative response to surface warming in the east Pacific alone, i.e., $\frac{\Delta R_{global\_EP}}{\Delta T_{global\_WP}+\Delta T_{global\_other}}$. The orange line ("Rest") shows the estimated feedback using the radiative response to surface warming in the rest of the globe, i.e., $\frac{\Delta R_{global\_other}}{\Delta T_{global\_WP}+\Delta T_{global\_other}}$. In panel (b) and (d), γ is calculated as $\Delta T_{global\_other}/\Delta T_{global\_WP}$ (Eq. 21), both terms are 10-years running averages.

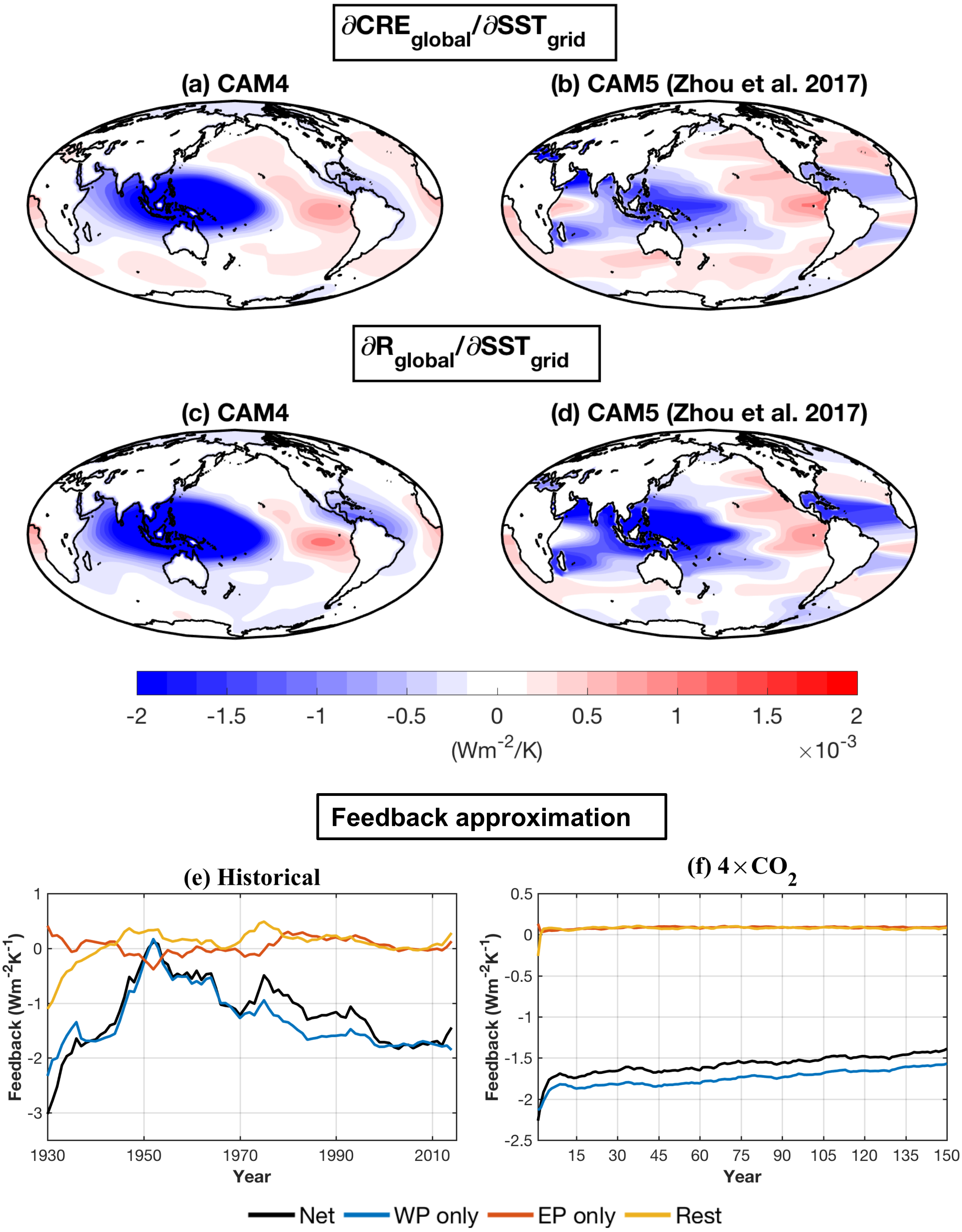

Figure 11: Comparison of results from this study with those from the CAM5 Green's function in Zhou et al. (2017). Panel (a, b) shows global-mean cloud radiative effect (CRE) change to unit SST warming in each grid box (unit: Wm^{-2}/K). Panel (c, d) shows global-mean net TOA

radiation change to a unit SST warming in each grid box (unit: Wm^{-2}/K). The left column shows results from CAM4 (this study), the right column shows results from CAM5 (Zhou et al. 2017). Note that panel (c) is identical to panel (a) in Fig. 5. Panel (e, f) show the evolution of feedbacks estimated from the CAM5 Green's function, for (e) the *Historical* run and for (f) the $4{\times}CO_2$ run, to be compared to in Fig 10 (a, c). The "Net" feedback is estimated using the Green's function from Zhou et al. (2017). Note that CRE is slightly different to R_{cloud} used in Zhou et al. (2017); it is defined as the difference between net TOA radiation and clearsky net TOA radiation, without removing the cloud masking effect.

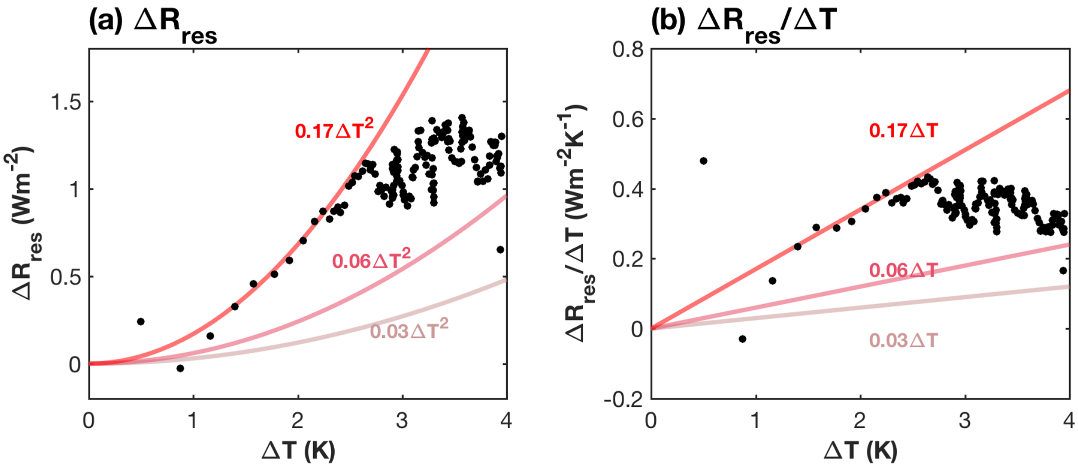

Figure 12: Nonlinear TOA radiation residual (ΔR_{res}) from the *4×CO₂* simulation. ΔR_{res} is the difference in global-mean net TOA radiation produced by model and those produced by the Green's function (unit: Wm^{-2}). Panel (a) shows the relationship of ΔR_{res} against global-mean TAS change (ΔT, unit: K); panel (b) shows the relationship of $\Delta R_{res}/\Delta$T ($Wm^{-2}K^{-1}$) against ΔT. The black dots are running 10-years averages from the *4×CO₂* simulation. The red lines in panel (a) and panel (b) denote quadratic relationship $\Delta R_{res} = b\Delta T^2$ and linear relationship $\Delta R_{res}/\Delta T = b\Delta T$, respectively, using b of 0.03 $Wm^{-2}K^{-2}$ (from Meraner et al. 2013), 0.06 $Wm^{-2}K^{-2}$ (from Roe and Armour, 2011), and 0.17 $Wm^{-2}K^{-2}$ (best-fitting for the data points over the first few decades).